ACS NANO

www.acsnano.org

ARTICLE

Tunable 1D and 2D Polyacrylonitrile Nanosheet Superstructures

Huaxin Gong, Diego Uruchurtu Patino, Jan Ilavsky, Ivan Kuzmenko, Amnahir Estefania Peña-Alcántara, Chenhui Zhu, Aidan H. Coffey, Lukas Michalek, Ahmed Elabd, Xin Gao, Shucheng Chen, Chengyi Xu, Hongping Yan, Yuanwen Jiang, Weichen Wang, Yucan Peng, Yitian Zeng, Hao Lyu, Hanul Moon, and Zhenan Bao*

Cite This: *ACS Nano* 2023, 17, 18392–18401

Read Online

ACCESS | Metrics & More | Article Recommendations | Supporting Information

ABSTRACT: **Carbon superstructures are widely applied in energy and environment-related areas. Among them, the flower-like polyacrylonitrile (PAN)-derived carbon materials have shown great promise due to their high surface area, large pore volume, and improved mass transport. In this work, we report a versatile and straightforward method for synthesizing one-dimensional (1D) nanostructured fibers and two-dimensional (2D) nanostructured thin films based on flower-like PAN chemistry by taking advantage of the nucleation and growth behavior of PAN. The resulting nanofibers and thin films exhibited distinct morphologies with intersecting PAN nanosheets, which formed through rapid nucleation on existing PAN. We further constructed a variety of hierarchical PAN superstructures based on different templates, solvents, and concentrations. These PAN nanosheet superstructures can be readily converted to carbon superstructures. As a demonstration, the nanostructured thin film exhibited a contact angle of ∼180° after surface modification with fluoroalkyl monolayers, which is attributed to high surface roughness enabled by the nanosheet assemblies. This study offers a strategy for the synthesis of nanostructured carbon materials for various applications.**

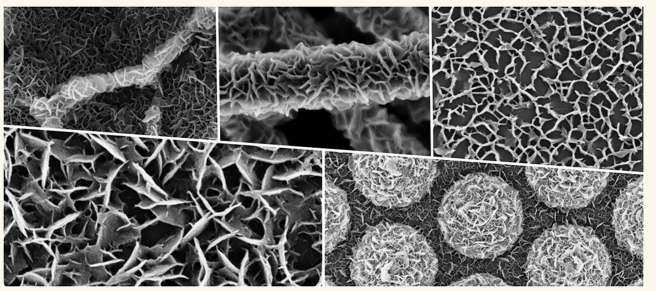

KEYWORDS: *Nanosheet, Nanofiber, Polyacrylonitrile, Crystallization, Superhydrophobic*

Carbon materials with three-dimensional (3D) superstructures have received great interest due to their advantageous properties such as high surface area, tunable pore size and structure, adjustable surface property, chemical stability, thermal conductivity, and electric conductivity. These characteristics allow carbon superstructures to play crucial roles in various applications such as batteries,[1−4] catalysis,[5−7] supercapacitors,[8−11] gas storage,[12−14] purification and separation.[15−18] Typically, carbon superstructures are synthesized by pyrolyzing small molecules or polymer precursors. Polyacrylonitrile (PAN) is a commonly used polymer carbon source for this purpose.[19] For instance, PAN-based carbon fibers account for more than 90% of global carbon fiber production.[20,21] PAN's unique cyclization reaction, occurring at around 250 °C, forms a ladder polymer structure that stabilizes the nano and microstructures of the material during high-temperature pyrolysis, resulting in well-controlled morphologies and excellent carbon yields.[20,21] In addition, the abundant nitrogen (N) atoms in the polymer backbone can be retained in PAN-derived carbon, enabling further surface modification and catalytic activity. The mild free-radical polymerization conditions of acrylonitrile also provide opportunities to incorporate various comonomers and inorganic salts into the polymer, tuning the chemical and physical structures of PAN-derived carbon materials.[22,23] Consequently, PAN and PAN-derived carbon superstructures have been extensively studied, exhibiting promising performance in numerous applications.[19]

Various strategies have been reported for the synthesis of PAN superstructures. One prominent method involves the fabrication of 1D PAN nanofibers by electrospinning. By adjusting the electrospinning conditions, PAN nanofibers of varying diameters can be easily fabricated. These free-standing PAN nanofiber cloths have found extensive use in environmental and energy applications.[24] Furthermore, the copoly-

Received: June 26, 2023
Accepted: August 25, 2023
Published: September 5, 2023

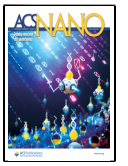

https://doi.org/10.1021/acsnano.3c05792
ACS Nano 2023, 17, 18392−18401

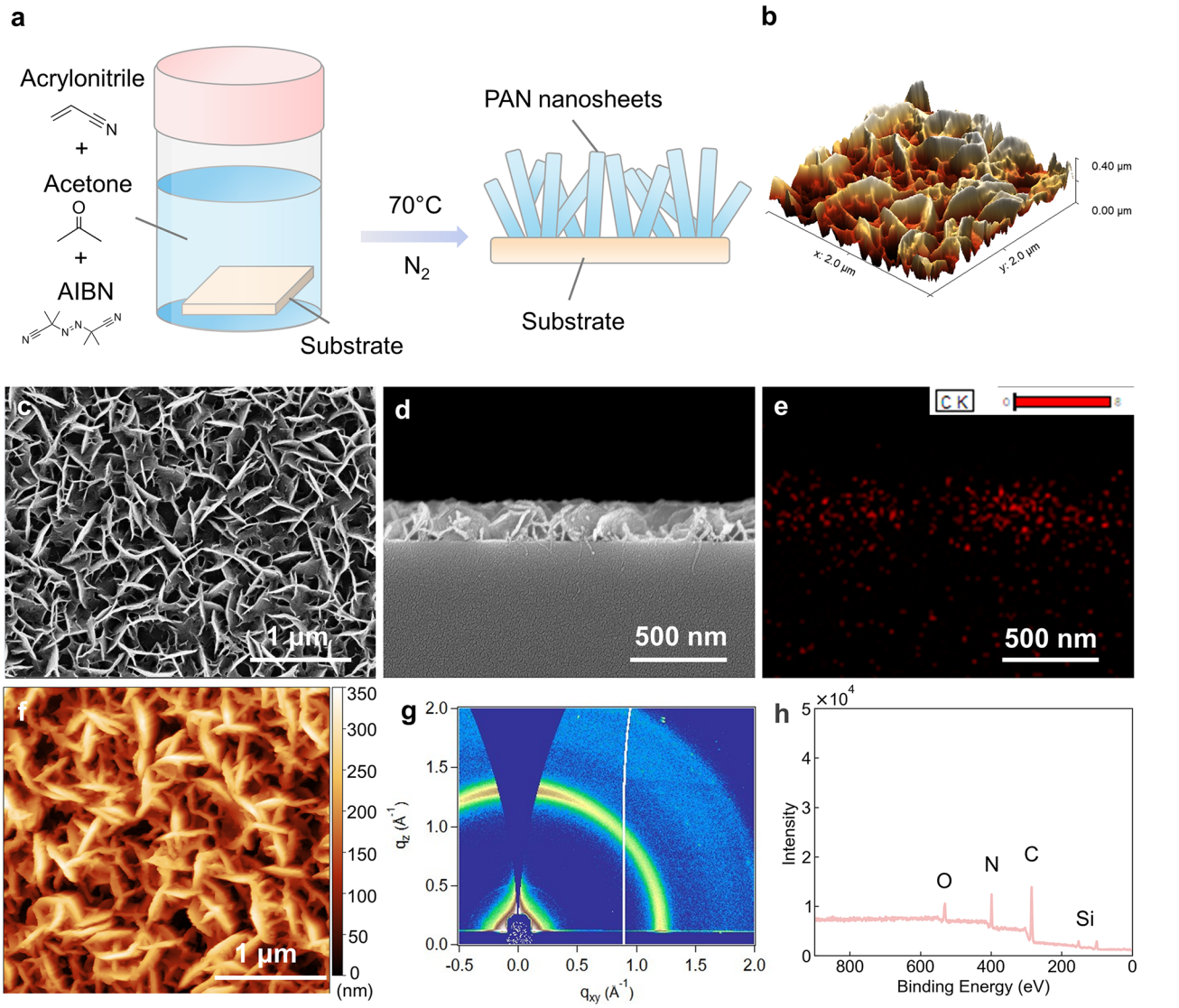

Figure 1. Synthesis and structures of 2D PAN nanosheet superstructures. (a) Schematic of the synthesis process of PAN nanosheet arrays. (b) 3D topography of PAN nanosheet arrays constructed by AFM. (c) SEM image of the surface morphology of PAN nanosheet arrays. (d) SEM image of the cross-sectional morphology of PAN nanosheet arrays. (e) EDX mapping of the cross-sectional morphology of PAN nanosheet arrays. (f) AFM image of the surface morphology of PAN nanosheet arrays. (g) GIWAXS pattern of PAN nanosheet arrays. (h) XPS of PAN nanosheet arrays on a Si wafer.

merization of acrylonitrile with other monomers can generate a range of PAN-containing block copolymers. Phase separation of the immiscible blocks can lead to diverse nanostructure morphologies, which is extensively used to produce 2D nanostructured PAN thin films.[25,26] Moreover, self-assembly of PAN-containing block copolymer micelles can be utilized to produce nanostructured PAN particles.[27,28] Templating methods, which are capable of producing both 2D and 3D superstructures, have also been reported.[29−31] The use of templates like silica enables precise control over the pore size of the PAN superstructures.[31] However, many of the PAN and carbon superstructures require complex synthesis procedures, which increase the cost and limit their large-scale production.[19] In our recent work, we reported flower-like PAN and its carbon derivatives, which are particularly appealing due to their simple synthesis process.[32,33] Meanwhile, these flower-like PAN superstructures have shown great potential due to their advantages, such as improved mass transport and more exposed active sites.[34−39] The flower-like PAN superstructures are formed due to the self-assembly of PAN nanosheets.[33] Nonetheless, the particles are typically spherical, although they offer advantages such as easy processing and dense packing in specific applications. Developing tunable flower-like PAN superstructures beyond spherical particles would allow more versatile applications in a broader range.

Here we report strategies for tuning the superstructures of PAN by controlling the self-assembly process of PAN nanosheets during synthesis. We successfully assembled PAN nanosheets into 1D nanofibers and 2D thin films. These superstructures could be readily synthesized in a one-pot reaction and tuned by synthesis conditions. Their structures and formation process were characterized by techniques such as grazing-incidence wide-angle X-ray scattering (GIWAXS), atomic force microscopy (AFM), ultrasmall-angle + small-angle X-ray scattering (USAXS + SAXS), and scanning electron microscopy (SEM). Moreover, the 2D nanostructured thin films enabled a contact angle close to 180°, demonstrating the potential of the obtained structures for superhydrophobicity.

https://doi.org/10.1021/acsnano.3c05792
ACS Nano 2023, 17, 18392−18401

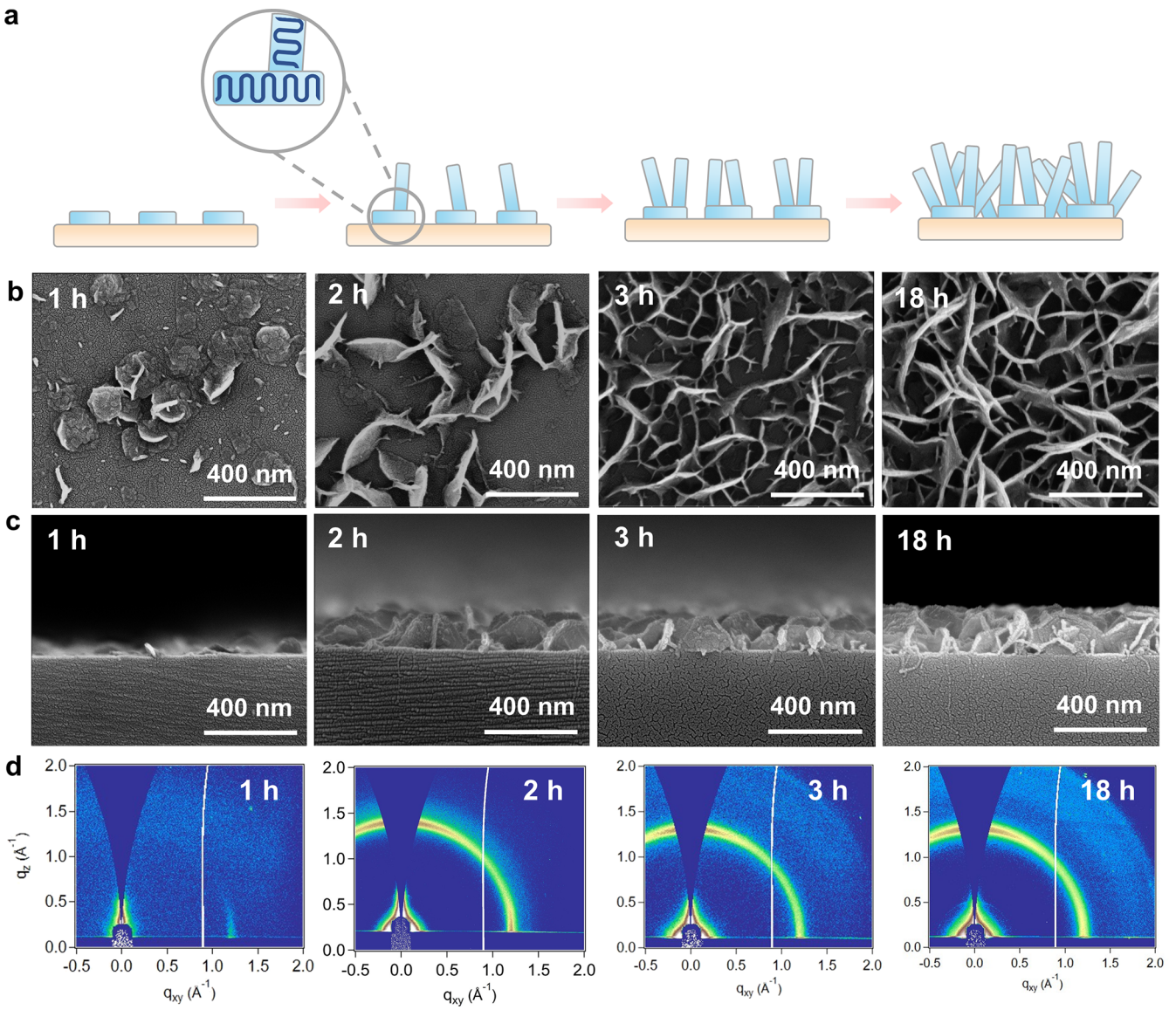

Figure 2. Structure evolution of 2D PAN nanosheet arrays. (a) Schematic illustration of the structural evolution of 2D PAN nanosheet arrays. (b) SEM images showing the structure evolution of 2D PAN nanosheet arrays. (c) GIWAXS patterns showing the structure evolution of 2D PAN nanosheet arrays.

RESULTS

Synthesis of 2D Thin Film Composed of PAN Nanosheets. In our previous reports, we studied the formation of flower-like PAN particles during free-radical polymerization of acrylonitrile in acetone.[32,33] Here, building upon this chemistry, we prepared 2D PAN nanosheet arrays instead of spherical particles, as shown Figure 1a. Detailed synthesis procedures can be found in the Methods section. Typically, a plasma-cleaned substrate was immersed in the monomer solution to grow PAN nanosheets during free-radical polymerization. The substrate was then removed and cleaned by sonication to detach excess PAN particles on the surface. Figure 1b presents a 3D topography of the surface-deposited PAN nanosheet arrays in a $2 \times 2\ \mu m^2$ area, collected using AFM. The 2D superstructures possessed a 9.5 μm^2 surface area in a $2 \times 2\ \mu m^2$ area measured by AFM, an ~84 nm root−mean−square (RMS) roughness, and a ~1 GPa Derjaguin-Muller-Toporov (DMT) modulus (Figure S1). SEM imaging (Figure 1c) revealed that the nanosheets intersected with each other and created pores between them. The substantially increased surface area and roughness may be beneficial in various applications such as batteries,[40] supercapacitors,[41] superhydrophobic surfaces,[42] and surface-enhanced Raman scattering (SERS).[43] Cross-sectional SEM imaging (Figure 1d), energy-dispersive X-ray spectroscopy (EDX) mapping (Figure 1e), and AFM imaging (Figure 1f) additionally confirmed that the nanosheets were primarily vertically aligned with a height of ~300 nm. Interestingly, the height of the nanosheet arrays seemed to be self-limited to this value, determined by the size of the PAN crystals. The nanosheets generated a bright scattering ring in the GIWAXS pattern (Figure 1g), corresponding to the primary diffraction peak of crystalline PAN at $d \approx 5.3$ Å.[33] Meanwhile, the intensity of the ring was stronger in the low azimuthal angle region near the q_z axis, indicating that the polymer chains oriented parallel to the surface of the substrate, in the nanosheets that grew in the normal direction on the surface.[44] The nanosheets observed here is similar to our previous report.[33] The chemical composition of the nanosheet arrays was characterized by X-

https://doi.org/10.1021/acsnano.3c05792
ACS Nano 2023, 17, 18392−18401

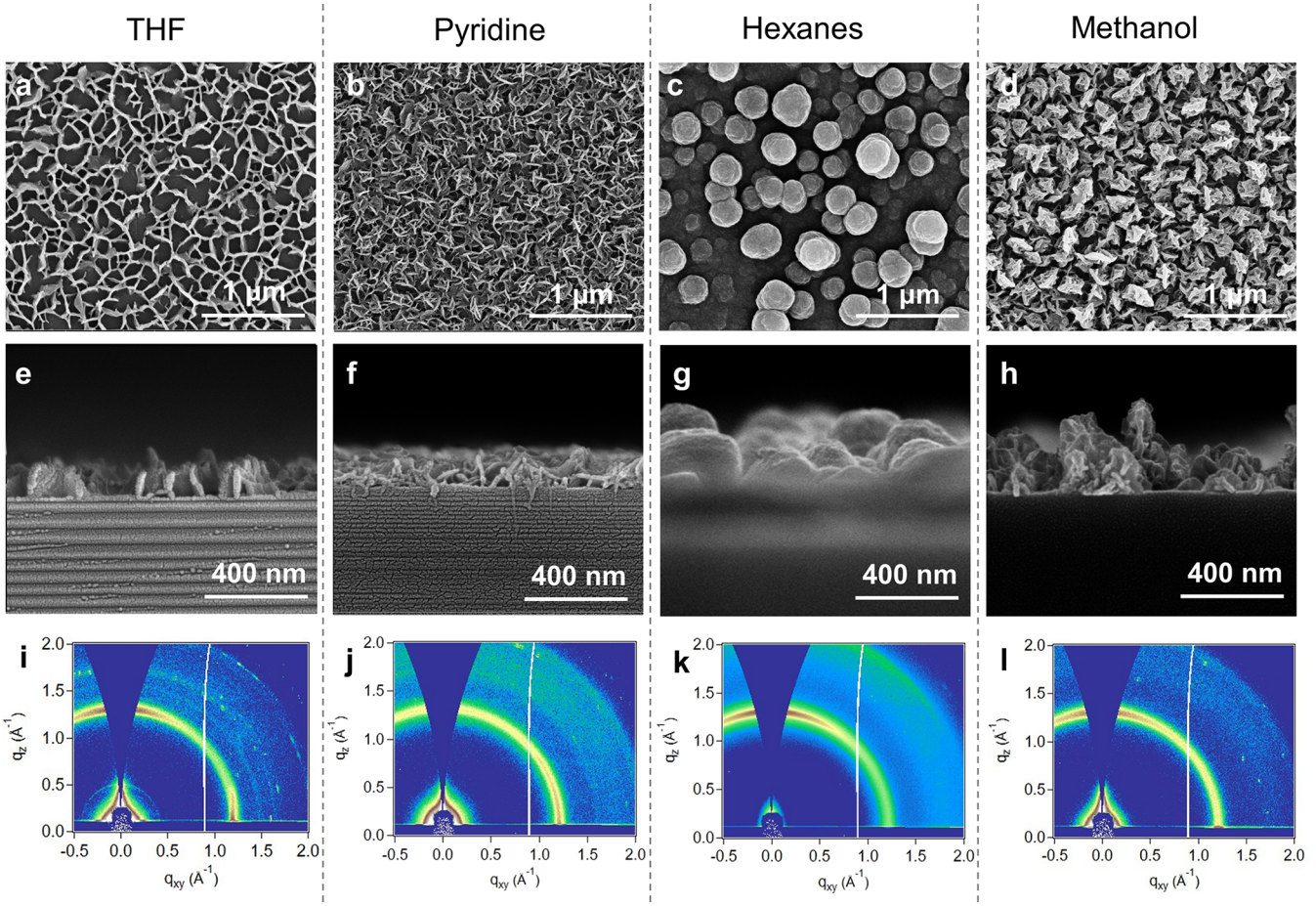

Figure 3. Solvent effects on the morphology of PAN nanosheet arrays. (a–d) SEM images of surface morphology of PAN nanosheet arrays synthesized from various solvents. (e–h) SEM images of cross-sectional morphology of PAN nanosheet arrays synthesized from different solvents. (i–l) GIWAXS patterns of PAN nanosheet arrays synthesized from different solvents.

ray photoelectron spectroscopy (XPS), where the C and N signals were observed, attributed to the PAN structure (Figure 1h). Additionally, strong Si and O signals were observed, indicating that the nanosheets did not completely cover the silicon substrate surface. The PAN nanosheets can be further converted into carbon nanosheets through stabilization and carbonization processes as previously reported (Figure S2).

Formation Process of 2D PAN Nanosheet Arrays. The formation process of the nanosheets was investigated using ex situ SEM imaging and GIWAXS. Specifically, the reaction time was controlled at 1, 2, 3, and 18 h, and the substrates with PAN nanosheets were then removed for characterization. Figure 2a presents a schematic of the hypothesized growth process of the nanosheet arrays. Figure 2b–d display the corresponding SEM images of the surface morphology, cross-sectional morphology, and GWAXS pattern of the PAN nanosheet arrays at different stages of the reaction. At the early stage of reaction, PAN nanosheets were observed to predominantly grow parallel to the silicon substrate surface, resulting in the formation of numerous thin disks as depicted in Figure 2b. This observation can be further correlated by the GIWAXS pattern (Figure 2d) of the 1 h samples showing PAN chains oriented perpendicular to the surface. Since PAN chains were believed to fold in a zigzag configuration within the nanosheets, this gives their orientations being primarily perpendicular to the substrate surface. Consequently, the GIWAXS signal is mainly from the q_{xy} axis. Such a growth behavior may be due to the high surface energy of the Si wafer after O_2 plasma treatment. It is possible that the abundant dangling bonds on the surface could potentially react with free radicals and help anchor the PAN chains. Alternatively, the PAN chains may prefer to minimize their interactions with the substrate surface and result in vertical growth. As a result, the PAN chains vertically aligned and formed face-on crystals. As the reaction time increased, additional PAN crystals began to nucleate and grow primarily perpendicular to the existing ones. Therefore, the substrate surface began covered by a mixture of face-on and edge-on PAN nanosheets, leading to the GIWAXS intensity growing stronger both in the q_z and q_{xy} directions. Later, the substrate surface was almost entirely covered by nanosheets and additional vertically oriented PAN nanosheets formed by branching of the existing nanosheets. The stronger intensity along the q_z direction in the corresponding GIWAXS pattern further confirmed the predominantly edge-on orientation of the nanosheets. Finally, the size of the nanosheets and the height of the 2D superstructures significantly increased with a longer growth time. Meanwhile, although the majority of the nanosheets were vertically oriented, more random orientations of the nanosheets were observed in the plane parallel to the substrate surface, as shown in the SEM images and reduced anisotropy in the GIWAXS pattern.

Tuning the Morphology of PAN Nanosheet Arrays. In our previous work, we reported that solvents play critical roles in the morphology of the PAN particles. A variety of shapes such as leaf-like and flower-like particles were obtained by conducting

https://doi.org/10.1021/acsnano.3c05792
ACS Nano 2023, 17, 18392–18401

reactions in different solvents.[32] Here, we also observed that solvent can substantially alter the morphology and orientation of the PAN nanosheets. The 2D superstructures showed distinctly different morphologies when synthesized from different solvents. For example, the vertically aligned PAN nanosheets synthesized in tetrahydrofuran (THF) exhibited a more perpendicular orientation, as seen in the SEM images (Figure 3a,e). The corresponding GIWAXS pattern showed stronger intensity along the q_z and q_{xy} directions, indicating the coexistence of both face-on and edge-on orientations (Figure 3i). The flower-like spherical particles formed in the solution were less dense (Figure S3). Interestingly, when pyridine was used as the solvent, the flower-like particles formed in the solution were denser. The nanosheets had a smaller size, and their orientations were more random with a slightly higher face-on orientation (Figure 3b,f). This observation can be seen in the strong signal along different azimuth angles in the ring and slightly stronger intensity near the q_{xy} axis in the GIWAXS pattern (Figure 3j). This is possibly due to the smaller PAN crystal size produced in pyridine. The larger space between these small crystals allows PAN nanosheets to branch in different directions. Additionally, PAN particles polymerized in hexanes gave aggregations of nanospheres without nanosheets both in solution and on the silicon substrate (Figures S3 and 3c,g). Interestingly, polymer chains in the nanosphere arrays still exhibited preferential orientation. As illustrated by Figure 3k, the stronger signal along the q_z direction indicated that the polymer chains were stacked parallel to the substrate surface, similar to the aforementioned vertically aligned nanosheets. Lastly, the 2D thin film superstructures were composed of leaf-like nanosheet aggregates when synthesized in methanol. The leaf-like aggregates appeared as individual islands on the substrate surface with a more random orientation compared to the structures derived in THF (Figure 3d,h,l). The heights of the leaf-like superstructures were more inhomogeneous. The above results indicated that solvent could substantially influence the nucleation and growth of PAN crystals. In addition to solvents, the concentration of the monomer was seen to influence the density of nanosheets on the substrate (Figure S5).

Synthesis of 1D Nanostructured Fibers Composed of PAN Nanosheets. Building on the aforementioned observation that PAN nanosheets can grow on substrate interfaces, we further explored their growth onto 1D nanofibers. We employed a similar synthetic process but used the already stabilized PAN nanofibers as the substrate (Figure 4a). The resulting nanostructured fibers consisted of a nanofiber core and a shell with PAN nanosheets. We first prepared electrospun PAN nanofibers and stabilized them at 230 °C to serve as templates for growing PAN nanosheets. The bare nanofibers had smooth surfaces with ~200 nm diameters (Figure 4b,f). After the reaction, numerous PAN nanosheets intersected and grew on the bare nanofibers, forming nanostructured nanofibers (Figure 4c,g). The diameters of the nanostructured fiber could be readily tuned by altering the size of the nanofiber templates (Figure S6). Moreover, these nanostructured fibers could be further stabilized and carbonized to create hierarchical porous carbon fibers (Figure 4d,e,h,i). The intersecting nanofibers formed free-standing cloths, making them promising for various applications such as electrodes in batteries, supercapacitors, fuel cells, and membranes in purification and separation.

We characterized the nanofiber cloths using USAXS + SAXS (Figure 4j,k). In Figure 4j, starting from the right side of the scattering pattern, a small broad peak was observed at $Q \approx 0.4$ Å^{-1}, corresponding to a feature size of ~1.5 nm. This small feature was attributed to the microvoids produced during the stabilization process of PAN, which were previously reported to be formed by gas evolution inside the fiber.[45] However, at the same Q range after nanosheet growth (Figure 4k), the broad peak disappeared, likely because the microvoids were filled up by PAN during the nanosheet growth reaction. The disappearance of microvoid features in SAXS had also been observed previously when filling micropores of carbon materials.[46] Meanwhile, a new peak at $Q \approx 1.2$ Å^{-1} appeared in Figure 4k, corresponding to the primary diffraction peak of crystalline PAN.[33] Moving to the left (Figure 4j(ii)), a sloping region with Q^{-4} power law corresponded to the Porod region of the smooth surfaces of the electrospun nanofibers. In contrast, the power law is $Q^{-3.4}$ in the same region of Figure 4k(ii), indicating fractal surfaces structure rather than smooth surfaces and the fractal dimension is 2.6, consistent with our previous report on flower-like PAN.[33] At $Q \approx 0.1$ Å^{-1} of Figure 4k(i), a small shoulder appeared, corresponding to the thickness of the PAN nanosheets (~8 nm) according to our previous assignment.[33] Further to the left (Figure 4j,k(iii)), another shoulder and a small valley were observed, corresponding to the Guinier region and the first oscillation valley of the Porod region. Fitting this part of the curve provided size distributions of the nanofibers, with results that were consistent with the SEM images. Specifically, the region in Figure 4j could be fitted to a cylinder model with a 220

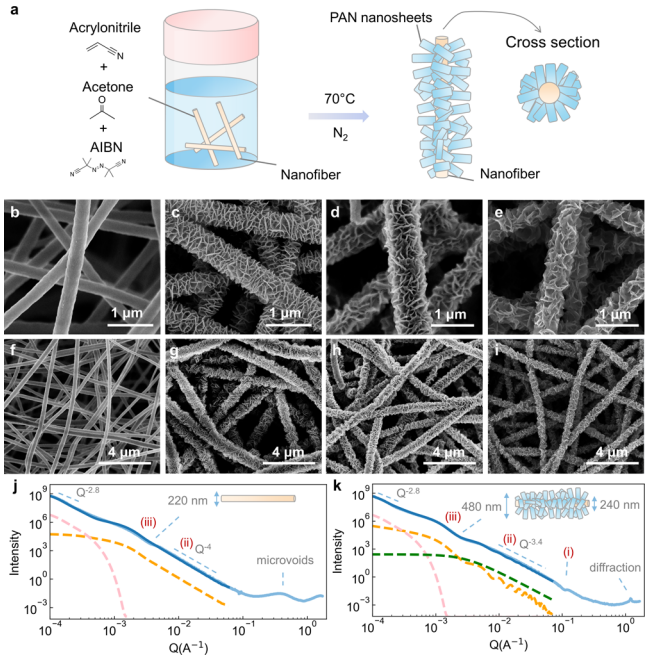

Figure 4. Synthesis and structures of 1D PAN nanosheet superstructures. (a) Schematic synthetic process of PAN nanosheets coated fibers. (b, f) SEM image of bare PAN nanofibers after stabilization. (c, g) SEM image of nanostructured fibers coated by PAN nanosheets. (d, h) Nanostructured fibers after stabilization. (e, i) Nanostructured fibers after carbonization. (j) USAXS + SAXS curve of bare nanofiber. Light blue curve: raw data. Dark blue curve: summation of modeling results. Yellow dashed line: cylinder form factor model. Pink dashed line: mass fractal model. (k) USAXS + SAXS curve of nanostructured fibers coated by PAN nanosheets. Light blue curve: raw data. Dark blue curve: summation of modeling results. Yellow dashed line: core−shell cylinder form factor model. Pink dashed line: mass fractal model. Green dashed line: surface fractal model.

https://doi.org/10.1021/acsnano.3c05792
ACS Nano 2023, 17, 18392−18401

± 70 nm diameter. In Figure 4k, the shoulder and valley were fitted by a core−shell cylinder model with a 240 ± 120 nm diameter core and a 120 nm thick shell ($\rho_{shell} = 1/6\ \rho_{core}$). The leftmost part of the USAXS curves had a sloping region with $Q^{-2.8}$ power law, corresponding to a mass fractal structure. This is because, at >10 μm length scale, the intersecting nanofiber in the cloth can be considered as a mass fractal. Our USAXS + SAXS study provides useful insights for future research involving similar structures.

Additional Superstructures Based on PAN Nanosheets. The PAN nanosheets could be further deposited into various configurations by utilizing different templates. For instance, PAN nanosheet arrays could also grow on various other surfaces, such as on Al foil, exhibiting similar structures to those formed on Si wafers (Figure 5a). Commercial fibers, such as polypropylene (PP) fibers in masks, could also serve as templates. As a result, they can be easily coated with a layer of PAN nanosheets (Figure 5b). Upon removing the PP fiber core with *p*-xylene, microtubes composed of PAN nanosheets were created (Figures 5c and S8). By using templates with microstructures and nanostructures, more complex hierarchical structures could be achieved. For example, when anodic aluminum oxide (AAO) was used as the template, the PAN nanosheets grew on the solid part of AAO, creating hierarchical pore structures (Figure 5d). Figure 5e shows PAN nanosheets growing on sapphire microsphere arrays, resulting in a cabbage-like morphology. Another example is the superstructures of PAN nanosheets formed on laser-induced carbon (Figure 5f). The thick sheets correspond to the original laser-induced carbon. Numerous small nanosheets grew on the large sheets, forming hierarchical structures that span multiple length scales. The versatile superstructures composed of PAN nanosheets can be potentially leveraged for a wide range of applications.

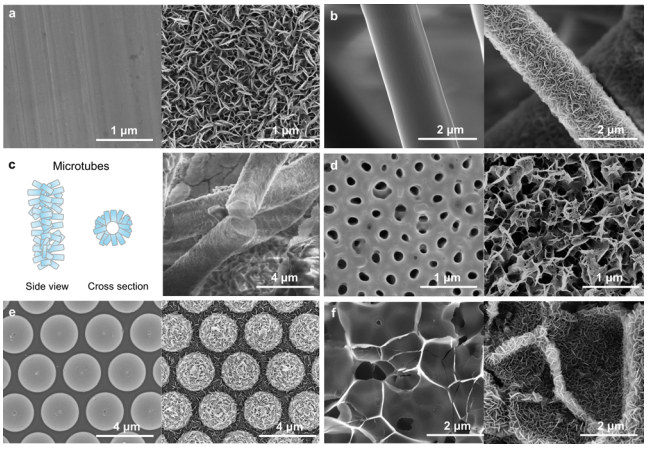

Figure 5. Various superstructures generated by PAN nanosheets. (a) SEM image of Al foil (left) and PAN nanosheets on Al foil (right). (b) SEM image of PP fiber (left) and PAN nanosheets on PP fiber (right). (c) Schematic and SEM image of hollow microtubes composed of PAN nanosheets. (d) SEM image of AAO (left) and PAN nanosheets on AAO (right). (e) SEM image of sapphire microsphere arrays (left) and PAN nanosheets on sapphire microsphere arrays (right). (f) SEM image of laser-induced carbon (left) and PAN nanosheets on laser-induced carbon (right).

Superhydrophobic Surface Enabled by PAN Nanosheet Arrays. As an application of the superstructures derived from PAN nanosheets, we employed the PAN nanosheet arrays to create superhydrophobic surfaces. The surfaces of the nanosheet arrays were modified using the widely reported gold−thiol chemistry.[47] Typically, a 10−20 nm thin layer of Au was first thermally evaporated onto the surface of PAN nanosheet arrays. Subsequently, these arrays were grafted with a monolayer by immersing them in an isopropanol (IPA) solution of 12,12,13,13,14,14,15,15,16,16,17,17,18,18,19,19,19-heptadecafluorononadecanethiol for 20 min, resulting in PANS-AuFSH (Figure 6a). The significant increase in surface roughness, enabled by the vertically oriented nanosheets, led to a substantial improvement in the contact angle of the surface of PANS-AuFSH. In comparison to a smooth surface with evaporated gold, which had a contact angle of ∼135° after monolayer modification (Figure 6b,c), the contact angle of PANS-AuFSH reached ∼180° (Figure 6d,e). The surface of the superhydrophobic PANS-AuFSH showed no observable affinity to water. Figure 6f and Supporting Video 1 show our attempts to attach a water droplet to the PANS-AuFSH surface. Even when the droplet was pressed onto the surface, it exhibited no adhesion when being extracted. Furthermore, water droplets could not rest on the horizontal surface of the PANS-AuFSH surface. As seen in Supporting Video 2, when water droplets were injected onto the surface of PANS-AuFSH, they immediately rolled off in a random direction. This near-zero adhesion made it challenging to measure the contact angle with a sessile drop, so we used a pendant drop instead (Figure 6e). We also employed the method reported by McCarthy and co-workers[48,49] (Figure 6g) to measure the contact angle. There was no observable affinity of the water droplet to the substrate, indicating a "perfectly" hydrophobic surface. Such large enhancements of the hydrophobicity can be attributed to the small dimensions of the PAN nanosheets. The thickness of the nanosheets is ∼8 nm, which is significantly smaller compared to many reported nanostructures produced from methods such as lithography. The high aspect ratio of the nanosheets also facilitated the trapping of air in between the intersecting superstructures and the formation of Cassie's superhydrophobic

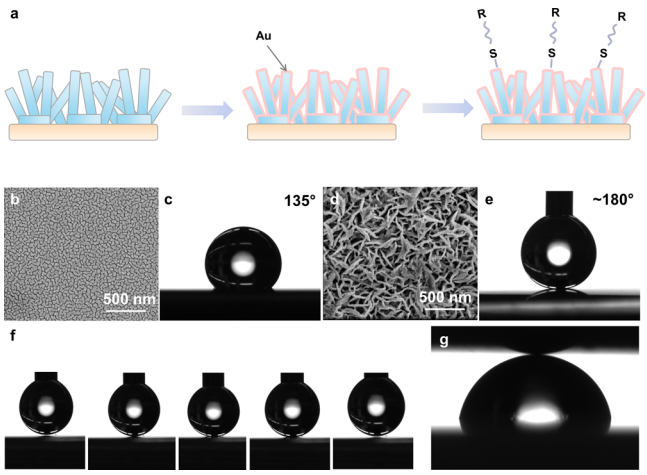

Figure 6. Superhydrophobic surface enabled by PAN nanosheet arrays. (a) Schematic showing the preparation procedure for superhydrophobic PANS-AuFSH surface. (b) SEM image of a ∼20 nm Au-coated Si wafer. (c) Contact angle of Au-coated Si wafer after monolayer modification. (d) SEM image of ∼20 nm Au-coated PAN nanosheet arrays. (e) Contact angle of PANF-AuFSH. (f) Images showing the process of attaching and detaching a water droplet on the PANF-AuFSH surface. (g) PANF-AuFSH surface in contact with a sessile drop, demonstrating near zero adhesion.

https://doi.org/10.1021/acsnano.3c05792
ACS Nano 2023, 17, 18392−18401

state.[42,50,51] In contrast, the surface treated with fluorine-free molecules (1-octadecanethiol) demonstrated a smaller contact angle (~145°), indicating the importance of fluorination. The contact angle measured on the Au and fluorinated alkythiol-treated nanosphere arrays was only ~123°, highlighting the advantages of the nanosheet superstructures (Figure S9). In our system, the hydrophobic nature arises from two distinct mechanisms: 1. the 2D PAN nanostructures, which enhance the surface roughness significantly, and 2. the fluoroalkyl monolayers, which anchor onto the surface via gold−thiol bonds. It is worth noting that the PAN nanostructures have demonstrated stability over extended periods, thus underpinning the hydrophobicity's robustness mainly to the stability of the gold−thiol bonds. We recognize, as previously reported, that the gold−thiol bond can undergo various decomposition pathways depending on the environmental conditions.[52] However, for the PANF-AuFSH samples discussed in our study, they were typically stored in an atmospheric environment without explicit control over humidity and temperature. Characterizations were routinely performed within 2 weeks post the monolayer modification. During this observation window, we did not detect any observable decline in the samples' hydrophobicity. Moreover, the nanosheet superstructures can be formed on various substrates using simple synthesis process, making them promising for superhydrophobic applications such as anticorrosion, antifogging, oil/water separation, self-cleaning, water harvesting, and more. In addition to superhydrophobic applications, the Au-coated superstructures also demonstrated promising SERS effects (Figure S11).

CONCLUSIONS

In conclusion, we report that PAN nanosheets could be deposited onto a variety of substrates such as 1D nanofibers, 2D thin films, and various hierarchical structures. During the deposition process, we observed that the nanosheets first tend to grow on the surface in a face-on orientation, followed by edge-on growth. The solvents used in the reaction were found to significantly influence the morphology and orientation of the PAN nanosheets. PANF-AuFSH surface, based on PAN nanosheet superstructures, demonstrate near 180° contact angles, which is rarely reported. The highly tunable superstructures, along with the versatility and adaptability of this method, offer significant potential in various applications.

METHODS

Chemical Information. Acrylonitrile (≥99%, contains 35−45 ppm monomethyl ether hydroquinone as inhibitor), commercial polyacrylonitrile (average Mw 150,000), 2,2′-Azobis(2-methylpropionitrile) (AIBN, 98%), methyl methacrylate (MMA, contains ≤30 ppm methyl 2-methylpropenoate as inhibitor, 99%), and pyridine were purchased from Sigma-Aldrich. Acetone (ACS, 99.5+%), tetrahydrofuran (THF), methanol, hexanes, and *N*,*N*-dimethylformamide (DMF) were purchased from Thermo Scientific.

Synthesis of PAN Nanosheets Superstructures. Typically, a mixture of 3 mL of acrylonitrile, 15 mL of acetone, and 5 mg of AIBN was prepared. An O_2-plasma-treated substrate (Plasma Etch PE-50, maximum power for 1 min), such as a Si wafer, was immersed in the solution. The solution was then purged with N_2 for ~1 min, sealed, and reacted at 70 °C overnight. Upon completion of the reaction, the solution turned into a white suspension. The substrate was removed, bath sonicated in acetone, and rinsed with acetone 2−3 times to eliminate PAN particles adhered to the surface. The reaction was halted at different time intervals to examine the structural evolution of PAN nanosheets.

For the solvent effect study, acetone was replaced with THF, pyridine, hexanes, or methanol, while other reaction conditions remained the same. The PAN nanosheet superstructures were heated up to 230 °C in the air for 2 h for stabilization, followed by carbonization at 600 °C in N_2 (70 sccm/min) for another 2 h.

For the synthesis of nanofibers, a mixture of 1.9 mL of acrylonitrile, 0.1 mL of MMA, 2 mL of acetone, and 2 mg of AIBN was prepared and purged with N_2. The solution was then heated to 70 °C overnight. The resulting polymer product was dried and dissolved in DMF to create a 5 wt % solution. The PAN solution was electrospun under 15 kV voltage, a 15 cm distance, and a 1.5 mL/h extrusion rate. The electrospun fabrics were removed from the collector and stabilized at 230 °C in air for 2 h. Next, the stabilized fabrics were then used as a substrate to grow PAN nanosheets. The reaction conditions were the same as those for PAN arrays grown on Si wafers.

For the synthesis of different hierarchical superstructures, AAO, Al foil, PP fiber, sapphire microsphere arrays, and laser-induced carbon were utilized as substrates to grow hierarchical structures. The laser-induced carbon was prepared on the surface of a polyimide film by irradiating a CO_2 infrared laser with a power of 15% and a writing speed of 30% (Epilog Fusion M2). Then a solution of SEBS (150 mg/mL in toluene, Asahi Kasei Tuftec H1062) was drop-casted over the laser-induced carbon structures and left overnight to fully remove the solvent. Last, the cured SEBS elastomer was delaminated from the polyimide substrate with the laser-induced carbon structures completely transferred and embedded on the SEBS surface. The reaction conditions were the same as those for PAN arrays grown on Si wafers.

Fabrication of Superhydrophobic Surface. The PAN nanosheet array-coated substrate was coated with a 10−20 nm layer of Au by thermal evaporation at a rate of ~10 Å/s. Following this, the Au-coated substrate was immersed in an IPA solution containing 0.25 mg/mL of 12,12,13,13,14,14,15,15,16,16,17,17,18,18,19,19,19-heptadecafluorononadecanethiol for 20 min. Afterward, the substrate was rinsed with IPA and dried using an air gun.

GIWAXS Characterization. GIWAXS spectra were taken at beamline 7.3.3. at the advanced light source (ALS) at Lawrence Berkeley National Lab with a 10 keV beam. 2D spectra were recorded with a Pilatus 2M-2D detector.

USAXS + SAXS Characterization. USAXS + SAXS experiments were conducted at the 20-ID-B beamline at the Advanced Photon Source of Argonne National Laboratory with 21 keV X-ray energy. Beam size is 0.8 × 0.8 mm^2 for USAXS and 0.8 × 0.2 mm^2 for SAXS. Exposure time is 90 s for USAXS and 20 s for SAXS. The flux density is approximately 1 × 10^{12} photons/(s mm^2).[53−57] USAXS data were reduced using instrument data reduction software provided by beamline and SAXS data were reduced using Nika.[57] Data were corrected for the instrumental background as well as appropriate sample container scattering. All USAXS data presented are desmeared. Fitting is conducted with the Modeling tool of Irena[58−62] to understand the particle shape and size distribution. Cylinder form factor[63] with Gaussian distribution, core−shell cylinder form factor with Gaussian distribution,[63] unified level model (mass fractal fitting),[64] and surface fractal model[64] were used for fitting.

Microscopy Imaging and Other Material Characterizations. SEM images and EDX mapping were collected by an FEI Magellan 400 XHR Scanning Electron Microscope at Stanford Nano Shared Facilities (SNSF). All polymer samples were coated with <1 nm Au/Pd (60:40) to alleviate the charging effects of insulating polymers. AFM measurements were collected using a Bruker Icon Dimension instrument with a SCANASYST-AIR probe (from Bruker AFM Probes, USA with a nominal spring constant of 0.4 N/m, resonance frequency of 70 kHz, and a tip radius of 2 nm) at SNSF. Nanomechanical maps were recorded in the Peak Force Quantitative Nanomechanics (PF-QNM) mode while scanning on a homogeneous area of the film surface. All nanomechanical images were recorded at a set point of ~1 nN with a Peak Force frequency of 2 kHz and amplitude of 150 nm. The scan resolution was set to 256 × 256 pixel with a scan-rate of 0.3 Hz. The data were evaluated and depicted with Gwyddion SPM software, which was also used to generate the histograms through a 1D statistical function to estimate the apparent DMT-modulus. XRD data were

https://doi.org/10.1021/acsnano.3c05792
ACS Nano 2023, 17, 18392−18401

collected by an Empyrean X-ray Diffractometer from PANalytical with a Cu source at SNSF. XPS spectra were collected on a VersaProbe 4 XPS (Physical Electronics, Inc.) at SNSF. Contact angles were measured by a Rame-Hart 290 Contact Angle Goniometer at SNSF. Raman spectra were collected by Horiba XploRA$^+$ Confocal Raman at SNSF with 638 nm laser (1.07 mW) and 1800 gr/mm grating. Liquid samples for SERS are prepared by dropping 20 μL 0.1 mg/mL Rhodamine 6G (R6G) aqueous solution on a substrate and covered by a cover glass.

ASSOCIATED CONTENT

Supporting Information

The Supporting Information is available free of charge at https://pubs.acs.org/doi/10.1021/acsnano.3c05792.

Video of attempts to attach a water droplet to the PANS-AuFSH surface (MP4)

Video of water droplets injected onto the surface of PANS-AuFSH (MP4)

Additional SEM, AFM, XPS, Raman, XRD, N_2 physisorption, and contact angle data (PDF)

AUTHOR INFORMATION

Corresponding Author

Zhenan Bao − *Department of Chemical Engineering, Stanford University, Stanford, California 94305, United States;* orcid.org/0000-0002-0972-1715; Email: zbao@stanford.edu

Authors

Huaxin Gong − *Department of Chemical Engineering, Stanford University, Stanford, California 94305, United States;* orcid.org/0000-0002-2493-0793

Diego Uruchurtu Patino − *Department of Chemical Engineering, Stanford University, Stanford, California 94305, United States*

Jan Ilavsky − *Advanced Photon Source, Argonne National Laboratory, Lemont, Illinois 60439, United States;* orcid.org/0000-0003-1982-8900

Ivan Kuzmenko − *Advanced Photon Source, Argonne National Laboratory, Lemont, Illinois 60439, United States*

Amnahir Estefania Peña-Alcántara − *Department of Materials Science and Engineering, Stanford University, Stanford, California 94305, United States*

Chenhui Zhu − *Advanced Light Source, Lawrence Berkeley National Laboratory, Berkeley, California 94720, United States*

Aidan H. Coffey − *Advanced Light Source, Lawrence Berkeley National Laboratory, Berkeley, California 94720, United States*

Lukas Michalek − *Department of Chemical Engineering, Stanford University, Stanford, California 94305, United States*

Ahmed Elabd − *Department of Chemical Engineering, Stanford University, Stanford, California 94305, United States*

Xin Gao − *Department of Materials Science and Engineering, Stanford University, Stanford, California 94305, United States;* orcid.org/0000-0001-5360-0796

Shucheng Chen − *Department of Chemical Engineering, Stanford University, Stanford, California 94305, United States;* orcid.org/0000-0002-1420-099X

Chengyi Xu − *Department of Chemical Engineering, Stanford University, Stanford, California 94305, United States*

Hongping Yan − *Department of Chemical Engineering, Stanford University, Stanford, California 94305, United States*

Yuanwen Jiang − *Department of Chemical Engineering, Stanford University, Stanford, California 94305, United States*

Weichen Wang − *Department of Materials Science and Engineering, Stanford University, Stanford, California 94305, United States*

Yucan Peng − *Department of Materials Science and Engineering, Stanford University, Stanford, California 94305, United States*

Yitian Zeng − *Department of Materials Science and Engineering, Stanford University, Stanford, California 94305, United States;* orcid.org/0000-0002-6949-8033

Hao Lyu − *Department of Chemical Engineering, Stanford University, Stanford, California 94305, United States*

Hanul Moon − *Department of Chemical Engineering, Stanford University, Stanford, California 94305, United States*

Complete contact information is available at: https://pubs.acs.org/10.1021/acsnano.3c05792

Notes

The authors declare no competing financial interest.

ACKNOWLEDGMENTS

This research was supported by the U.S. Department of Energy, Office of Science, Office of Basic Energy Sciences, Chemical Sciences, Geosciences, and Biosciences Division, Catalysis Science Program to the SUNCAT Center for Interface Science and Catalysis. A.P.A. acknowledges support from the National Science Foundation Graduate Research Fellowship Program under Grant No. DGE-1656518 as well as the Stanford Knight−Hennessy Scholarship and the Stanford Enhancing Diversity in Graduate Education Doctoral Fellowship. L.M. gratefully acknowledges funding through the Walter Benjamin Fellowship Programme by the Deutsche Forschungsgemeinschaft (DFG 456522816). Part of this work was performed at the Stanford Nano Shared Facilities (SNSF), supported by the National Science Foundation under award ECCS-2026822. This research used resources of the Advanced Light Source, which is a DOE Office of Science User Facility under Contract No. DE-AC02-05CH11231. This research used resources of the Advanced Photon Source, a U.S. Department of Energy (DOE) Office of Science User Facility operated for the DOE Office of Science by Argonne National Laboratory under Contract No. DE-AC02-06CH11357.

REFERENCES

(1) Lin, D.; Liu, Y.; Liang, Z.; Lee, H.-W.; Sun, J.; Wang, H.; Yan, K.; Xie, J.; Cui, Y. Layered Reduced Graphene Oxide with Nanoscale Interlayer Gaps as a Stable Host for Lithium Metal Anodes. *Nat. Nanotechnol.* **2016**, *11* (7), 626−632.

(2) Pan, H.; Chen, J.; Cao, R.; Murugesan, V.; Rajput, N. N.; Han, K. S.; Persson, K.; Estevez, L.; Engelhard, M. H.; Zhang, J.-G.; Mueller, K. T.; Cui, Y.; Shao, Y.; Liu, J. Non-Encapsulation Approach for High-Performance Li−S Batteries through Controlled Nucleation and Growth. *Nat. Energy* **2017**, *2* (10), 813−820.

(3) Zhu, G.; Tian, X.; Tai, H.-C.; Li, Y.-Y.; Li, J.; Sun, H.; Liang, P.; Angell, M.; Huang, C.-L.; Ku, C.-S.; Hung, W.-H.; Jiang, S.-K.; Meng, Y.; Chen, H.; Lin, M.-C.; Hwang, B.-J.; Dai, H. Rechargeable Na/Cl2 and Li/Cl2 Batteries. *Nature* **2021**, *596* (7873), 525−530.

(4) Jain, R.; Lakhnot, A. S.; Bhimani, K.; Sharma, S.; Mahajani, V.; Panchal, R. A.; Kamble, M.; Han, F.; Wang, C.; Koratkar, N. Nanostructuring versus Microstructuring in Battery Electrodes. *Nat. Rev. Mater.* **2022**, *7* (9), 736−746.

(5) Chung, H. T.; Cullen, D. A.; Higgins, D.; Sneed, B. T.; Holby, E. F.; More, K. L.; Zelenay, P. Direct Atomic-Level Insight into the Active

Sites of a High-Performance PGM-Free ORR Catalyst. *Science* **2017**, *357* (6350), 479−484.
(6) Li, W.; Liu, J.; Zhao, D. Mesoporous Materials for Energy Conversion and Storage Devices. *Nat. Rev. Mater.* **2016**, *1* (6), 16023.
(7) Liu, D.; Li, X.; Chen, S.; Yan, H.; Wang, C.; Wu, C.; Haleem, Y. A.; Duan, S.; Lu, J.; Ge, B.; Ajayan, P. M.; Luo, Y.; Jiang, J.; Song, L. Atomically Dispersed Platinum Supported on Curved Carbon Supports for Efficient Electrocatalytic Hydrogen Evolution. *Nat. Energy* **2019**, *4* (6), 512−518.
(8) Xiong, G.; He, P.; Lyu, Z.; Chen, T.; Huang, B.; Chen, L.; Fisher, T. S. Bioinspired Leaves-on-Branchlet Hybrid Carbon Nanostructure for Supercapacitors. *Nat. Commun.* **2018**, *9* (1), 790.
(9) Zhou, Z.; Liu, T.; Khan, A. U.; Liu, G. Block Copolymer−Based Porous Carbon Fibers. *Science Advances* **2019**, *5* (2), No. eaau6852.
(10) Yin, J.; Zhang, W.; Alhebshi, N. A.; Salah, N.; Alshareef, H. N. Synthesis Strategies of Porous Carbon for Supercapacitor Applications. *Small Methods* **2020**, *4* (3), No. 1900853.
(11) Zhang, L. L.; Zhao, X. S. Carbon-Based Materials as Supercapacitor Electrodes. *Chem. Soc. Rev.* **2009**, *38* (9), 2520−2531.
(12) Morris, R. E.; Wheatley, P. S. Gas Storage in Nanoporous Materials. *Angew. Chem., Int. Ed.* **2008**, *47* (27), 4966−4981.
(13) Marco-Lozar, J. P.; Kunowsky, M.; Suárez-García, F.; Carruthers, J. D.; Linares-Solano, A. Activated Carbon Monoliths for Gas Storage at Room Temperature. *Energy Environ. Sci.* **2012**, *5* (12), 9833.
(14) Gadipelli, S.; Guo, Z. X. Graphene-Based Materials: Synthesis and Gas Sorption, Storage and Separation. *Prog. Mater. Sci.* **2015**, *69*, 1−60.
(15) Guan, W.; Guo, Y.; Yu, G. Carbon Materials for Solar Water Evaporation and Desalination. *Small* **2021**, *17* (48), No. 2007176.
(16) Chen, C.; Li, Y.; Song, J.; Yang, Z.; Kuang, Y.; Hitz, E.; Jia, C.; Gong, A.; Jiang, F.; Zhu, J. Y.; Yang, B.; Xie, J.; Hu, L. Highly Flexible and Efficient Solar Steam Generation Device. *Adv. Mater.* **2017**, *29* (30), No. 1701756.
(17) Yousefi, N.; Lu, X.; Elimelech, M.; Tufenkji, N. Environmental Performance of Graphene-Based 3D Macrostructures. *Nat. Nanotechnol.* **2019**, *14* (2), 107−119.
(18) Srimuk, P.; Su, X.; Yoon, J.; Aurbach, D.; Presser, V. Charge-Transfer Materials for Electrochemical Water Desalination, Ion Separation and the Recovery of Elements. *Nat. Rev. Mater.* **2020**, *5* (7), 517−538.
(19) Kopeć, M.; Lamson, M.; Yuan, R.; Tang, C.; Kruk, M.; Zhong, M.; Matyjaszewski, K.; Kowalewski, T. Polyacrylonitrile-Derived Nanostructured Carbon Materials. *Prog. Polym. Sci.* **2019**, *92*, 89−134.
(20) König, S.; Bauch, V.; Herbert, C.; Wego, A.; Steinmann, M.; Frank, E.; Buchmeiser, M. R. High-Performance Carbon Fibers Prepared by Continuous Stabilization and Carbonization of Electron Beam-Irradiated Textile Grade Polyacrylonitrile Fibers. *Macromol. Mater. Eng.* **2021**, *306* (12), No. 2100484.
(21) Frank, E.; Ingildeev, D.; Buchmeiser, M. R. 2 - High-Performance PAN-Based Carbon Fibers and Their Performance Requirements. In *Structure and Properties of High-Performance Fibers*; Bhat, G., Ed.; Woodhead Publishing: Oxford, 2017; pp 7−30. DOI: 10.1016/B978-0-08-100550-7.00002-4.
(22) Kowalewski, T.; Tsarevsky, N. V.; Matyjaszewski, K. Nanostructured Carbon Arrays from Block Copolymers of Polyacrylonitrile. *J. Am. Chem. Soc.* **2002**, *124* (36), 10632−10633.
(23) Ju, A.; Guang, S.; Xu, H. Effect of Comonomer Structure on the Stabilization and Spinnability of Polyacrylonitrile Copolymers. *Carbon* **2013**, *54*, 323−335.
(24) Nataraj, S. K.; Yang, K. S.; Aminabhavi, T. M. Polyacrylonitrile-Based Nanofibers—A State-of-the-Art Review. *Prog. Polym. Sci.* **2012**, *37* (3), 487−513.
(25) Tang, C.; Tracz, A.; Kruk, M.; Zhang, R.; Smilgies, D.-M.; Matyjaszewski, K.; Kowalewski, T. Long-Range Ordered Thin Films of Block Copolymers Prepared by Zone-Casting and Their Thermal Conversion into Ordered Nanostructured Carbon. *J. Am. Chem. Soc.* **2005**, *127* (19), 6918−6919.
(26) Zhong, M.; Tang, C.; Kim, E. K.; Kruk, M.; Celer, E. B.; Jaroniec, M.; Matyjaszewski, K.; Kowalewski, T. Preparation of Porous Nanocarbons with Tunable Morphology and Pore Size from Copolymer Templated Precursors. *Mater. Horiz.* **2014**, *1* (1), 121−124.
(27) Aqil, A.; Detrembleur, C.; Gilbert, B.; Jérôme, R.; Jérôme, C. Controlled RAFT Synthesis of Polyacrylonitrile-b-Poly(Acrylic Acid) Diblocks as Precursors of Carbon Nanocapsules with Assistance of Gold Nanoparticles. *Chem. Mater.* **2007**, *19* (9), 2150−2154.
(28) Tang, C.; Qi, K.; Wooley, K. L.; Matyjaszewski, K.; Kowalewski, T. Well-Defined Carbon Nanoparticles Prepared from Water-Soluble Shell Cross-Linked Micelles That Contain Polyacrylonitrile Cores. *Angew. Chem., Int. Ed.* **2004**, *43* (21), 2783−2787.
(29) Song, Y.; Song, X.; Wang, X.; Bai, J.; Cheng, F.; Lin, C.; Wang, X.; Zhang, H.; Sun, J.; Zhao, T.; Nara, H.; Sugahara, Y.; Li, X.; Yamauchi, Y. Two-Dimensional Metal−Organic Framework Superstructures from Ice-Templated Self-Assembly. *J. Am. Chem. Soc.* **2022**, *144* (38), 17457−17467.
(30) Roberts, A. D.; Lee, J.-S. M.; Wong, S. Y.; Li, X.; Zhang, H. Nitrogen-Rich Activated Carbon Monoliths via Ice-Templating with High CO2 and H2 Adsorption Capacities. *J. Mater. Chem. A* **2017**, *5* (6), 2811−2820.
(31) Lu, A.; Kiefer, A.; Schmidt, W.; Schüth, F. Synthesis of Polyacrylonitrile-Based Ordered Mesoporous Carbon with Tunable Pore Structures. *Chem. Mater.* **2004**, *16* (1), 100−103.
(32) Chen, S.; Koshy, D. M.; Tsao, Y.; Pfattner, R.; Yan, X.; Feng, D.; Bao, Z. Highly Tunable and Facile Synthesis of Uniform Carbon Flower Particles. *J. Am. Chem. Soc.* **2018**, *140* (32), 10297−10304.
(33) Gong, H.; Ilavsky, J.; Kuzmenko, I.; Chen, S.; Yan, H.; Cooper, C. B.; Chen, G.; Chen, Y.; Chiong, J. A.; Jiang, Y.; Lai, J.; Zheng, Y.; Stone, K. H.; Huelsenbeck, L.; Giri, G.; Tok, J. B.-H.; Bao, Z. Formation Mechanism of Flower-like Polyacrylonitrile Particles. *J. Am. Chem. Soc.* **2022**, *144* (38), 17576−17587.
(34) Gong, H.; Chen, S.; Ning, R.; Chang, T.-H.; Tok, J. B.-H.; Bao, Z. Densely Packed and Highly Ordered Carbon Flower Particles for High Volumetric Performance. *Small Science* **2021**, *1*, No. 2000067.
(35) Tsao, Y.; Gong, H.; Chen, S.; Chen, G.; Liu, Y.; Gao, T. Z.; Cui, Y.; Bao, Z. A Nickel-Decorated Carbon Flower/Sulfur Cathode for Lean-Electrolyte Lithium−Sulfur Batteries. *Adv. Energy Mater.* **2021**, *11*, No. 2101449.
(36) Gong, H.; Chen, Y.; Chen, S.; Xu, C.; Yang, Y.; Ye, Y.; Huang, Z.; Ning, R.; Cui, Y.; Bao, Z. Fast-Charging of Hybrid Lithium-Ion/Lithium-Metal Anodes by Nanostructured Hard Carbon Host. *ACS Energy Lett.* **2022**, *7*, 4417−4426.
(37) Koshy, D. M.; Chen, S.; Lee, D. U.; Stevens, M. B.; Abdellah, A. M.; Dull, S. M.; Chen, G.; Nordlund, D.; Gallo, A.; Hahn, C.; Higgins, D. C.; Bao, Z.; Jaramillo, T. F. Understanding the Origin of Highly Selective CO_2 Electroreduction to CO on Ni,N-doped Carbon Catalysts. *Angew. Chem., Int. Ed.* **2020**, *59* (10), 4043−4050.
(38) JK O'Neill, S.; Gong, H.; Matsuhisa, N.; Chen, S.; Moon, H.; Wu, H.; Chen, X.; Chen, X.; Bao, Z. A Carbon Flower Based Flexible Pressure Sensor Made from Large-Area Coating. *Adv. Mater. Interfaces* **2020**, *7* (18), No. 2000875.
(39) Chen, S.; Gong, H.; Dindoruk, B.; He, J.; Bao, Z. Dense Carbon Nanoflower Pellets for Methane Storage. *ACS Appl. Nano Mater.* **2020**, *3* (8), 8278−8285.
(40) Liu, Y.; Zhu, Y.; Cui, Y. Challenges and Opportunities towards Fast-Charging Battery Materials. *Nat. Energy* **2019**, *4* (7), 540−550.
(41) Frackowiak, E. Carbon Materials for Supercapacitor Application. *Phys. Chem. Chem. Phys.* **2007**, *9* (15), 1774−1785.
(42) Wang, S.; Liu, K.; Yao, X.; Jiang, L. Bioinspired Surfaces with Superwettability: New Insight on Theory, Design, and Applications. *Chem. Rev.* **2015**, *115* (16), 8230−8293.
(43) Vo-Dinh, T. Surface-Enhanced Raman Spectroscopy Using Metallic Nanostructures. *trends in analytical chemistry* **1998**, *17*, 557.
(44) Baker, J. L.; Jimison, L. H.; Mannsfeld, S.; Volkman, S.; Yin, S.; Subramanian, V.; Salleo, A.; Alivisatos, A. P.; Toney, M. F. Quantification of Thin Film Crystallographic Orientation Using X-Ray Diffraction with an Area Detector. *Langmuir* **2010**, *26* (11), 9146−9151.
(45) Lee, J.-E.; Chae, Y. K.; Lee, D. J.; Choi, J.; Chae, H. G.; Kim, T. H.; Lee, S. Microstructural Evolution of Polyacrylonitrile Fibers during

Industry-Mimicking Continuous Stabilization. *Carbon* **2022**, *195*, 165−173.
(46) Härk, E.; Ballauff, M. Carbonaceous Materials Investigated by Small-Angle X-Ray and Neutron Scattering. *C* **2020**, *6* (4), 82.
(47) Liu, K.; Jiang, L. Metallic Surfaces with Special Wettability. *Nanoscale* **2011**, *3* (3), 825−838.
(48) Gao, L.; McCarthy, T. J. A Perfectly Hydrophobic Surface (θ_A/θ_R = 180°/180°). *J. Am. Chem. Soc.* **2006**, *128* (28), 9052−9053.
(49) Gao, L.; McCarthy, T. J. A Commercially Available Perfectly Hydrophobic Material (θ_A/θ_R = 180°/180°). *Langmuir* **2007**, *23* (18), 9125−9127.
(50) Si, Y.; Dong, Z.; Jiang, L. Bioinspired Designs of Superhydrophobic and Superhydrophilic Materials. *ACS Cent. Sci.* **2018**, *4* (9), 1102−1112.
(51) Shibuichi, S.; Onda, T.; Satoh, N.; Tsujii, K. Super Water-Repellent Surfaces Resulting from Fractal Structure. *J. Phys. Chem.* **1996**, *100* (50), 19512−19517.
(52) Love, J. C.; Estroff, L. A.; Kriebel, J. K.; Nuzzo, R. G.; Whitesides, G. M. Self-Assembled Monolayers of Thiolates on Metals as a Form of Nanotechnology. *Chem. Rev.* **2005**, *105* (4), 1103−1170.
(53) Ilavsky, J.; Zhang, F.; Andrews, R. N.; Kuzmenko, I.; Jemian, P. R.; Levine, L. E.; Allen, A. J. Development of Combined Microstructure and Structure Characterization Facility for in Situ and Operando Studies at the Advanced Photon Source. *J. Appl. Crystallogr.* **2018**, *51* (3), 867−882.
(54) Ilavsky, J.; Jemian, P. R.; Allen, A. J.; Zhang, F.; Levine, L. E.; Long, G. G. Ultra-Small-Angle X-Ray Scattering at the Advanced Photon Source. *J. Appl. Crystallogr.* **2009**, *42* (3), 469−479.
(55) Ilavsky, J.; Allen, A. J.; Levine, L. E.; Zhang, F.; Jemian, P. R.; Long, G. G. High-Energy Ultra-Small-Angle X-Ray Scattering Instrument at the Advanced Photon Source. *J. Appl. Crystallogr.* **2012**, *45* (6), 1318−1320.
(56) Ilavsky, J.; Zhang, F.; Allen, A. J.; Levine, L. E.; Jemian, P. R.; Long, G. G. Ultra-Small-Angle X-Ray Scattering Instrument at the Advanced Photon Source: History, Recent Development, and Current Status. *Metall Mater. Trans A* **2013**, *44* (1), 68−76.
(57) Ilavsky, J. Nika: Software for Two-Dimensional Data Reduction. *J. Appl. Crystallogr.* **2012**, *45* (2), 324−328.
(58) *Irena | USAXS*; Argonne National Laboratory, 2022. https://usaxs.xray.aps.anl.gov/software/irena (accessed 02-28-2022).
(59) Ilavsky, J.; Jemian, P. R. Irena: Tool Suite for Modeling and Analysis of Small-Angle Scattering. *J. Appl. Crystallogr.* **2009**, *42* (2), 347−353.
(60) Zhang, F.; Ilavsky, J.; Long, G. G.; Quintana, J. P. G.; Allen, A. J.; Jemian, P. R. Glassy Carbon as an Absolute Intensity Calibration Standard for Small-Angle Scattering. *Metall Mater. Trans A* **2010**, *41* (5), 1151−1158.
(61) Nelson, A. Co-Refinement of Multiple-Contrast Neutron/X-Ray Reflectivity Data Using MOTOFIT. *J. Appl. Crystallogr.* **2006**, *39* (2), 273−276.
(62) Beaucage, G. Approximations Leading to a Unified Exponential/Power-Law Approach to Small-Angle Scattering. *J. Appl. Crystallogr.* **1995**, *28* (6), 717−728.
(63) Kline, S. R. Reduction and Analysis of SANS and USANS Data Using IGOR Pro. *J. Appl. Crystallogr.* **2006**, *39* (6), 895−900.
(64) Gadikota, G.; Zhang, F.; Allen, A. J. Towards Understanding the Microstructural and Structural Changes in Natural Hierarchical Materials for Energy Recovery: In-Operando Multi-Scale X-Ray Scattering Characterization of Na- and Ca-Montmorillonite on Heating to 1150 °C. *Fuel (Lond)* **2017**, *196*, 195−209.

https://doi.org/10.1021/acsnano.3c05792
ACS Nano 2023, 17, 18392−18401